

A Methodology for the Regional-Scale-Decomposed Atmospheric Water Budget: Application to a Simulation of the Canadian Regional Climate Model Nested by NCEP–NCAR Reanalyses over North America

SOLINE BIELLI AND RENÉ LAPRISE

Département des Sciences de la Terre et de l'Atmosphère, Université du Québec à Montréal, Montréal, Québec, Canada

(Manuscript received 2 February 2005, in final form 23 June 2005)

ABSTRACT

The purpose of this work is to study the added value of a regional climate model with respect to the global analyses used to drive the regional simulation, with a special emphasis on the nonlinear interactions between different spatial scales, focusing on the moisture flux divergence. The atmospheric water budget is used to apply the spatial-scale decomposition approach, as it is a key factor in the energetics of the climate. A Fourier analysis is performed individually for each field on pressure levels. Each field involved in the computation of moisture flux divergence is separated into three components that represent selected scale bands, using the discrete cosine transform. The divergence of the moisture flux is computed from the filtered fields. Instantaneous and monthly mean fields from a simulation performed with the Canadian Regional Climate Model are decomposed and allowed to separate the added value of the model to the total fields.

Results show that the added value resides in the nonlinear interactions between large (greater than 1000 km) and small (smaller than 600 km) scales. The main small-scale forcing of the wind is topographic, whereas the humidity tends to show more small scales over the ocean. The time-mean divergence of moisture flux is also decomposed into contributions from stationary eddies and transient eddies. Both stationary and transient eddies are decomposed into different spatial scales and show very different patterns. The time-mean divergence due to transient eddies is dominated by large-scale (synoptic scale) features with little small scales. The divergence due to stationary eddies is a combination of small- and large-scale terms, and the main small-scale contribution occurs over the topography.

The same decomposition has been applied to the NCEP–NCAR reanalyses used to drive the regional simulation; the results show that the model best reproduces the time-fluctuation component of the moisture flux divergence, with a correlation between the model simulation and the NCEP–NCAR reanalyses above 0.90.

1. Introduction

Atmospheric water plays a key role in the energetics of the earth's climate, in the radiation budget by interacting with the solar and terrestrial radiation, and also in the heat budget through latent heat exchanges via water phase changes. Improved understanding of the water cycle is necessary to better understand the hydrological cycle as well as its links and reactions to climate change. Precipitation is a difficult quantity to

simulate correctly because it is the result of multiple physical and dynamical processes. Precipitations produced as part of low-resolution (global) data assimilation show nonnegligible differences compared to in situ or remotely sensed observations, as precipitation is greatly influenced by topographic and small-scale surface forcing as well as regional mesoscale circulation. Moreover, precipitation can be viewed as a measure of the ability of a model to reproduce relevant features of the atmospheric water cycle. Finally, hydrological models require precipitation to calculate the runoff, and a better understanding of this field is necessary for a better representation of the water cycle in these models. The atmospheric water budget is thus chosen for scale decomposition in this study.

The first purpose of this work is to study the added

Corresponding author address: Dr. Soline Bielli, Département des Sciences de la Terre et de l'Atmosphère, Université du Québec à Montréal, Ouranos, 550 rue Sherbrooke Ouest, 19^e, Montréal, QC H3A 1B9, Canada.
E-mail: bielli.soline@uqam.ca

value provided by a regional climate model (RCM) with respect to the global analyses used to drive the regional simulation. The main factors that can contribute to the added value are 1) the nesting technique to impose the lateral boundary conditions, 2) the numerical discretization and truncation, 3) the nonlinear interactions between different scales, 4) the lower boundary forcing (topography, land surface properties, land–sea mask), and 5) the performance of physics parameterization. It is thought that the first factor may contribute negatively because of the general ill-posed nature of the lateral boundary value problem in nested models that may degrade the solution near the lateral boundary. The other factors, however, are expected to contribute positively to improve the simulations due to the higher resolution with associated reduction of the numerical truncation errors and increased bandwidth of resolved scales. The main objective of this paper is to assess the contribution of the third factor to the added value in the vertically integrated atmospheric water budget by using scale decomposition.

Spectral analysis as a scale-decomposition tool has been widely used for diagnostic studies of atmospheric global models (e.g., Boer and Shepherd 1983; Lambert 1984, 1987; Trenberth and Solomon 1993; Boer 1994), mainly to study quantities such as energy and enstrophy. Spectral analysis as a diagnostic tool for the analysis of the limited-area model has been much less used (e.g., Errico 1985, 1987; Denis et al. 2002a). As the regional domain is nonperiodic, care must be exercised when implementing scale decomposition using spectral analysis as it can result in misrepresentation of scales that are close to or larger than the domain size. Because of this nonperiodicity, there is no exact way of implementing Fourier decomposition in a limited-area domain (e.g., Laprise 2003). Several scale-decomposition methods that exist for limited-area domain are implemented by removing some trend across the regional domain to render the fields periodic. This trend has been defined for example by Errico (1985) as a linear trend in each direction, by Tatsumi (1986) as a sine component with the wavelength equal to 4 times the model domain, and by Chen and Kuo (1992) as the harmonic part of the field. More recently, Denis et al. (2002a,b) used the discrete cosine transform (DCT) to spectrally analyze limited-area model fields without subtracting any component. This method is equivalent to assuming two-dimensional mirror symmetry of the fields, thus making the sine component of the Fourier series disappear; compared to other methods, there is no subtraction of any trend component from the fields.

Van Tuyl and Errico (1989) have used spectral analysis to study scale interactions in a mesoscale model by

filtering fields into bands of wavenumbers and then calculating the time tendencies for each band. Spectral analyses of the tendencies were then used to study the scale interactions. They showed that small-scale forcing is dominated by topographic forcing and they noted little interaction between large and small scales. They also conclude that the small scales did not generate significantly large scales. Finally, they found that the self-interaction of large scales did not contribute significantly to the small scales.

Here we use a similar approach but we will be focusing on the vertically integrated water vapor budget and the scale interactions will be determined through examination of quadratic flux-like terms involving different scales. The quadratic terms will be evaluated on a map in the physical space in order to study the regional implications of scale interactions. The DCT will be applied to select different spatial scales in terms of the water budget. Instead of working with discrete wavenumbers as Lambert (1987), we opted to work with wavebands as van Tuyl and Errico (1989) in order to reduce the number of terms in the scale decomposition and facilitate their interpretation in the physical space. Indeed, as discussed later, we will be focusing on the quadratic term of the divergence of the moisture flux, and the scale decomposition will be composed of N^2 terms, with N being the number of spectral bands. Following Laprise (2003), three bands are chosen: the first band represents the very large scales that are not resolved by the RCM, the second band includes the scales that are resolved by both the RCM and its global large-scale driving data, and the third band accounts for the small scales that are only resolved by the RCM. Thus, only nine quadratic terms have to be considered in the decomposition.

The next section presents a description of the methodology and a brief description of the RCM. Section 3 presents the results. A discussion of the results as well as the effects of using pressure levels and time sampling will be presented in section 4. Section 5 summarizes the results and discusses future work.

2. Experimental design

a. The water budget and diagnostic methodology

The vertically integrated atmospheric water budget can be defined as (e.g., Peixoto and Oort 1992):

$$\partial_t \bar{q} = -\nabla \cdot \bar{\mathbf{F}} + E - P, \quad (1)$$

where the overbar represents vertical integration on the pressure levels. The vertical integral is written as

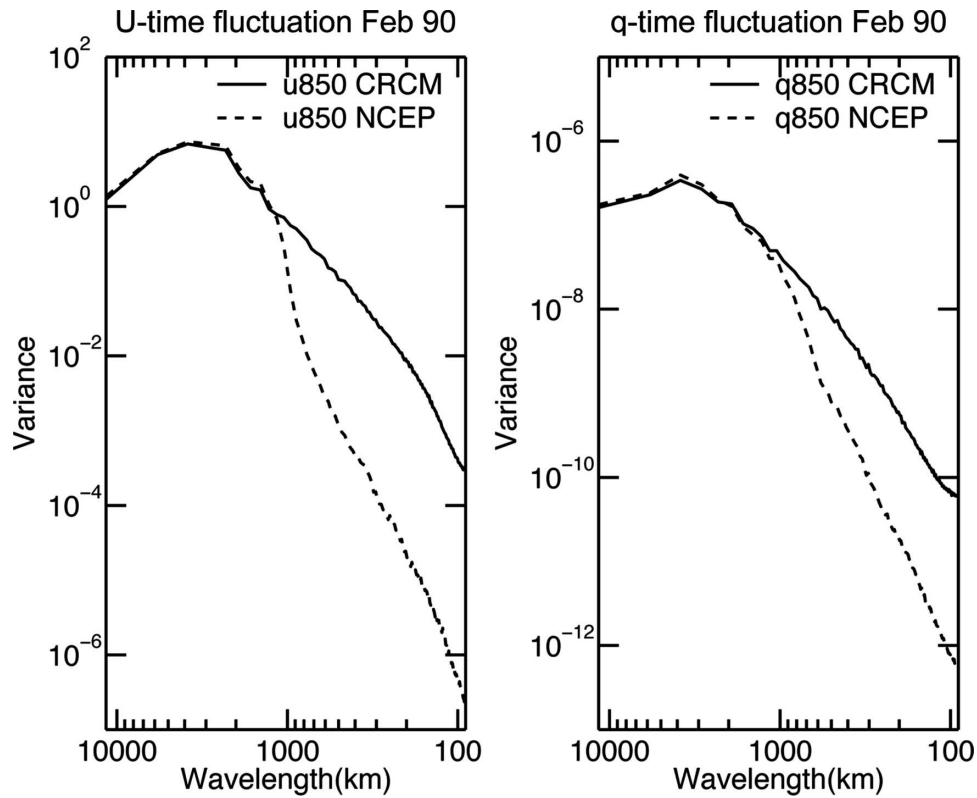


FIG. 1. Spectra of the time fluctuation of the wind and the specific humidity at 850 hPa for both CRCM and NCEP fields for the month of February 1990 over the North American domain shown in Fig. 3.

$$\bar{\psi} = \frac{1}{g} \int_{p_{\text{sfc}}}^{p_{\text{top}}} \psi dp \quad (2a)$$

with p_{top} and p_{sfc} , respectively, the lowest and the highest pressure values in a vertical atmospheric column. Here $\bar{\mathbf{F}}$ is the vertically integrated horizontal moisture flux, $\nabla \cdot \bar{\mathbf{F}}$ is the divergence of the moisture flux, $\nabla \cdot \bar{\mathbf{F}} = -\text{MFC}$ where MFC is the moisture flux convergence often used in the literature, q is the specific humidity, E is the evapotranspiration rate, and P is the precipitation rate. In this equation, the condensed atmospheric water has been neglected as it is very small at the scale used for this study, with a grid mesh of 45 km. Equation (2a) can be rewritten as

$$\bar{\psi} = \frac{1}{g} \int_{p_0}^{p_{\text{top}}} \beta \Psi dp, \quad (2b)$$

where the term β represents a mask based on unit function to take into account the topography in the lower boundary and p_0 is chosen as a value exceeding the maximum value of p_{sfc} in the domain (Boer 1982). This mask permits an unambiguous calculation of the diag-

nostic terms in the pressure coordinate. Note that β is computed on the Canadian Regional Climate Model (CRCM) grid, that is, with the high-resolution CRCM topography, even when applied to the National Centers for Environmental Prediction (NCEP) data.

Each term will be decomposed into three spatial scales and into two time components. To isolate the contribution of different spatial scales, spectral decomposition is applied to each term on pressure levels using DCT.

The divergence of the moisture flux, which is a quadratic term, is handled as follows. The specific humidity q is decomposed as $q = q_0 + q_L + q_S$ at each pressure level. The term q_0 represents the very large scales that are not resolved by the RCM (as a first approximation, it is defined as the domain-mean value; note that this definition differs from that of Laprise (2003) because it does not make the remaining part periodic), q_L represents the large scales that are resolved by both the RCM and the NCEP–National Center for Atmospheric Research (NCAR) reanalyses (scales larger than 1000-km wavelength), and q_S represents the small scales that are only resolved by the RCM (scales smaller than 600-km wavelength). Figure 1 displays the spectral variance

for the wind and humidity at 850 hPa for CRCM and NCEP data. It shows that NCEP starts to lose power around 1000-km wavelength compared to CRCM. This result motivates our choice of cutoff scale to separate q_L and q_S . A wavenumber spread is used in the DCT filter response to avoid an abrupt cutoff and thus reducing the Gibbs effects (see Denis et al. 2002a for more details). The spread is chosen such that the low-pass filter preserves all scales larger than 1000 km and the high-pass filter preserves all scales smaller than 600 km; in between, the response varies as a cosine square (Fig. 2). The same decomposition is applied to the individual components of the horizontal wind \mathbf{V} . The vertically integrated moisture flux is then calculated for each filtered field and the total flux is written as

$$\bar{\mathbf{F}} = \bar{\mathbf{F}}_0 + \bar{\mathbf{F}}_G + \bar{\mathbf{F}}_S \quad (3)$$

and

$$\begin{aligned} \bar{\mathbf{F}} &= \sum_a \sum_b \overline{\mathbf{V}_a q_b} = \overline{\mathbf{V}_0 q_0} + \overline{\mathbf{V}_0 q_L} \\ &+ \overline{\mathbf{V}_0 q_S} + \overline{\mathbf{V}_L q_0} + \overline{\mathbf{V}_L q_L} + \overline{\mathbf{V}_L q_S} \\ &+ \overline{\mathbf{V}_S q_0} + \overline{\mathbf{V}_S q_L} + \overline{\mathbf{V}_S q_S} \end{aligned} \quad (4)$$

with $(a, b) \in (0, L, S)$.

These nine components of the fluxes are evaluated in pressure coordinate, at each archival time, and then vertically integrated. Finally, the divergence $\nabla \cdot \bar{\mathbf{F}}$ of each of the nine terms is computed at each archival time with finite differences on the polar stereographic grid:

$$\nabla \cdot \bar{\mathbf{F}} = \nabla \cdot \overline{\mathbf{V}q} = S \left(\frac{\delta}{\delta x} \overline{uq} + \frac{\delta}{\delta y} \overline{vq} \right) \quad (5)$$

with S as the square of the map-scale factor. Note that the product of two terms contains scales that are both shorter and larger than those of the individual terms.

Another decomposition will be used to examine the results, which is a temporal decomposition defined as follows:

$$\psi = [\psi] + \psi' \quad \text{with} \quad \psi \in (\mathbf{V}, q, \mathbf{F}),$$

where $[\]$ represents temporal average. The time-mean vertically integrated moisture flux divergence $\nabla \cdot [\bar{\mathbf{F}}]$ is then composed of two elements:

$$\nabla \cdot [\bar{\mathbf{F}}] = [\nabla \cdot \bar{\mathbf{F}}] = \nabla \cdot [\overline{\mathbf{V}}[\overline{q}]] + \nabla \cdot [\overline{\mathbf{V}'q'}]. \quad (6)$$

The first term $\nabla \cdot [\overline{\mathbf{V}}[\overline{q}]]$ represents the contribution of stationary eddies, as it is the result of the time-mean wind and the time-mean humidity; the second term $\nabla \cdot [\overline{\mathbf{V}'q'}]$ represents the contribution of transient eddies, as is it the time mean of the product of the tran-

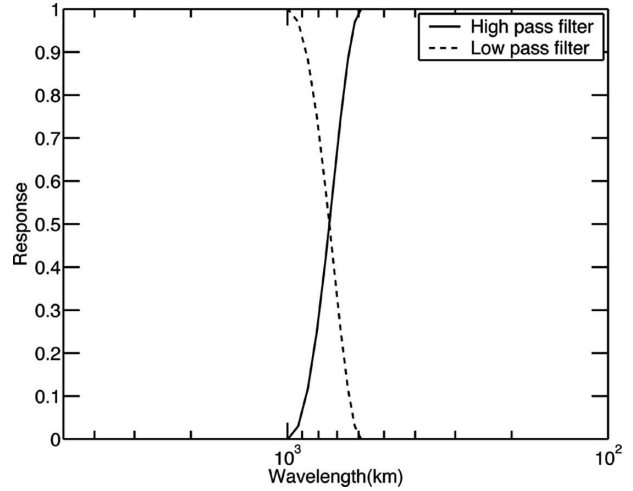


FIG. 2. Responses of the spectral filters used for low-pass and high-pass filtering of the fields for the scale decomposition.

sient wind with the transient humidity. Finally, we will also look at the standard deviation of the time fluctuation of the vertically integrated divergence defined as $\text{TF} = \sqrt{[(\nabla \cdot \bar{\mathbf{F}})]^2}$ to examine the time fluctuation in the moisture flux. For simplicity, in the following, TF_{ab} with $(a, b) \in (0, L, S)$ will represent the time fluctuation of the flux divergence involving the band a of the wind and the band b of the humidity field, that is $\text{TF}_{ab} = \sqrt{[(\nabla \cdot \mathbf{V}_a q_b)]^2}$.

b. The CRCM and its driving data

The CRCM, described by Caya and Laprise (1999), is used for this study. It is a fully elastic, nonhydrostatic, limited-area model that uses a semi-Lagrangian semi-implicit numerical scheme. The horizontal grid mesh used for this experiment is 45 km on a 192×144 grid-point polar stereographic computational domain. The model uses 29 Gal-Chen levels (Gal-Chen and Somerville 1975) in the vertical and the top of the domain is at 29 km. The lateral boundary conditions are provided through the one-way nesting method of Davies (1976), with a lateral sponge zone of nine points. The CRCM was driven by NCEP-NCAR reanalysis I (Kalnay et al. 1996) available every 6 h. Nudging of the wind was used for wavelengths greater than 1400 km and above the 500-hPa level. We suspect that the nudging has little influence on our results as the vertically integrated divergence of the moisture flux is mainly confined in the low levels where the humidity is maximum. The regional model subgrid-scale physical parameterization is similar to that used by Laprise et al. (2003). The simulation started in January 1973 and was run for 27 yr over a domain of about $6000 \text{ km} \times 8000 \text{ km}$ centered over Canada. For this paper, only one

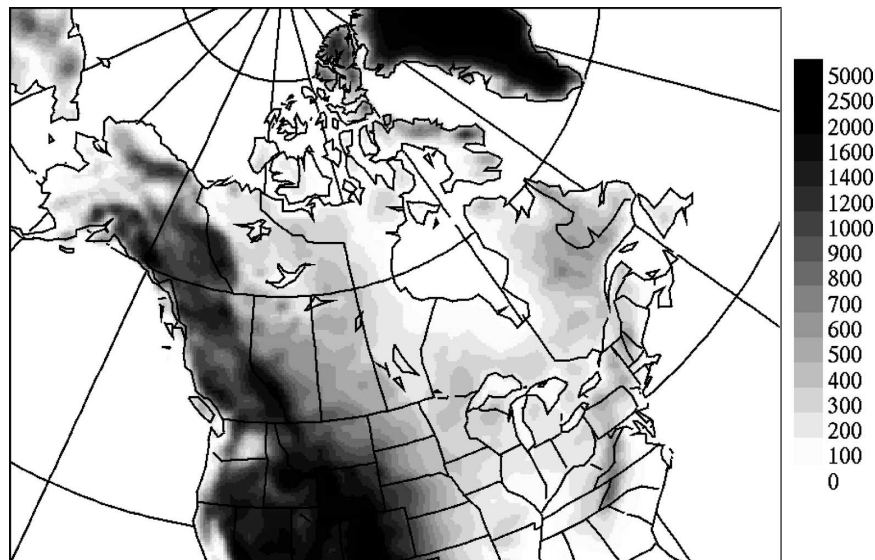


FIG. 3. Topography (m) and domain where the diagnostics are calculated.

winter month of this long simulation (February 1990) is used in order to study with care the methodological details before diagnosing the entire long simulation. The simulation outputs are interpolated on 30 pressure levels, 17 of which correspond to those of the NCEP–NCAR reanalysis, with 13 extra levels in the lower levels (below 700 hPa) to increase the vertical resolution for the moisture budget analysis and thus reduce the error associated with vertical interpolation. The NCEP–NCAR reanalyses have a resolution of $2.5^\circ \times 2.5^\circ$ and were interpolated on the CRCM 45-km horizontal grid. In the following, all the terms of the water budget are represented in units of millimeters per day and figures are shown on a central domain of 172×124 points (excluding a ribbon of 10 points from the computational domain representing the sponge zone). Figure 3 displays the topography in the inner domain (172×124 points) used for the diagnostic study. Three main mountainous regions cover this domain: the Rocky Mountains to the west of the domain, the Greenland mountains to the north of the domain with very strong gradient along the coast, and the Appalachian Mountains to the east, which are less elevated but nonetheless represent a nonnegligible forcing.

The CRCM-simulated atmospheric fields were archived at 6-hourly intervals, but surface fluxes, evapotranspiration, and precipitation were cumulated as time integrals between archival times. The water vapor tendency is evaluated as the difference between two archival times. The moisture flux divergence calculated on pressure levels with scale decomposition as described in previous section used instantaneous 6-hourly archival data.

For comparison, the horizontal moisture flux was also calculated on Gal-Chen levels during the integration of the model, at every time step, and cumulated between archival times. For this the water budget terms were computed on the so-called q points of the Arakawa-C grid. Thus the moisture flux divergence was approximated as $\nabla \cdot \mathbf{F} \approx \delta_x(\overline{u^x q^x}) + \delta_y(\overline{v^y q^y})$, where $\overline{u^x}$ and $\overline{v^y}$ represent centered averages, and δ_x and δ_y are centered finite differences. It is important to note that the spatial-scale decomposition would not make sense on Gal-Chen levels over topography. Therefore results involving Gal-Chen level computations will be produced for the total fields only.

3. Water budget and spatial decomposition of the moisture flux divergence

a. An instantaneous time at 1200 UTC 15 February 1990

1) WATER BUDGET TERMS

Before proceeding with the statistical analysis of the water budget, it is instructive to look at an instantaneous evaluation of the water budget, relating it to the weather situation of the moment. Figure 4 is showing the CRCM fields for mean sea level pressure (MSLP), the specific humidity at 850 hPa (q_{850}) and the horizontal wind at 850 hPa (\mathbf{V}_{850}) for 12 UTC 15 February 1990. The synoptic situation for this time is characterized by a quasi-stationary occluded depression on the Vancouver Island, with relatively dry air behind. Another depression is localized over Michigan and is moving northeastward bringing moist air over the east coast

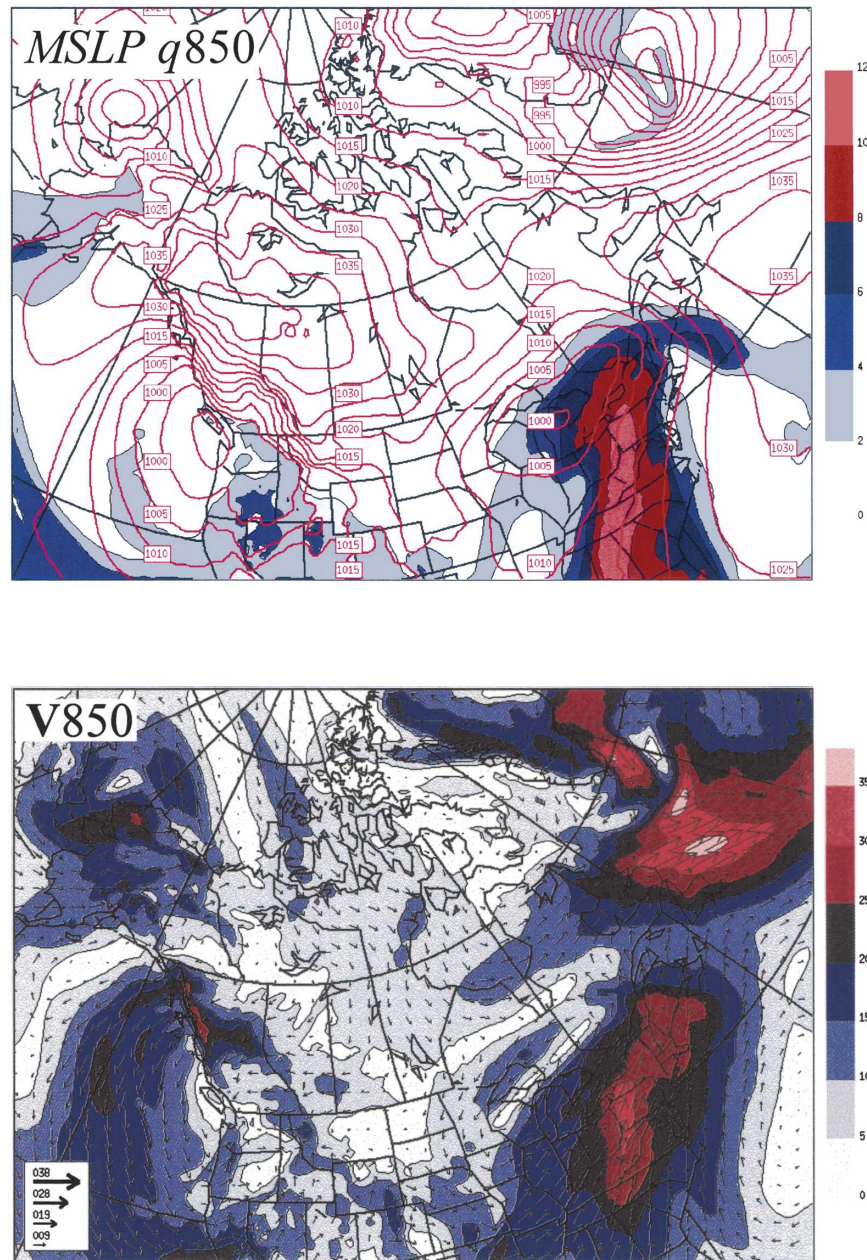


FIG. 4. (top) MSLP (contour, hPa) and specific humidity at 850 hPa (colored, mm day^{-1}). (bottom) Horizontal wind vector and speed (m s^{-1}) at 850 hPa for 1200 UTC 15 Feb 1990.

of North America. The four terms of the water budget [Eq. (1)] are displayed in Fig. 5. The vertically integrated divergence of the moisture flux shows two main structures: an elongated band of convergence just west of the east coast associated with a well-defined band of precipitation often observed during winter time; a dipole of convergence–divergence over the Pacific Ocean with a west–east orientation, which is mainly responsible for the water vapor tendency. It is interesting to

note that moisture flux divergence over the Gulf of St. Lawrence shows a convergence of moisture without precipitation. This has the effect of increasing the moisture content of the atmosphere as seen in the water vapor tendency field. On the other hand, the moisture convergence produces precipitation southwestward where the moisture saturation has been reached. The evapotranspiration term only shows a maximum off the Labrador coast associated with a cold continental air

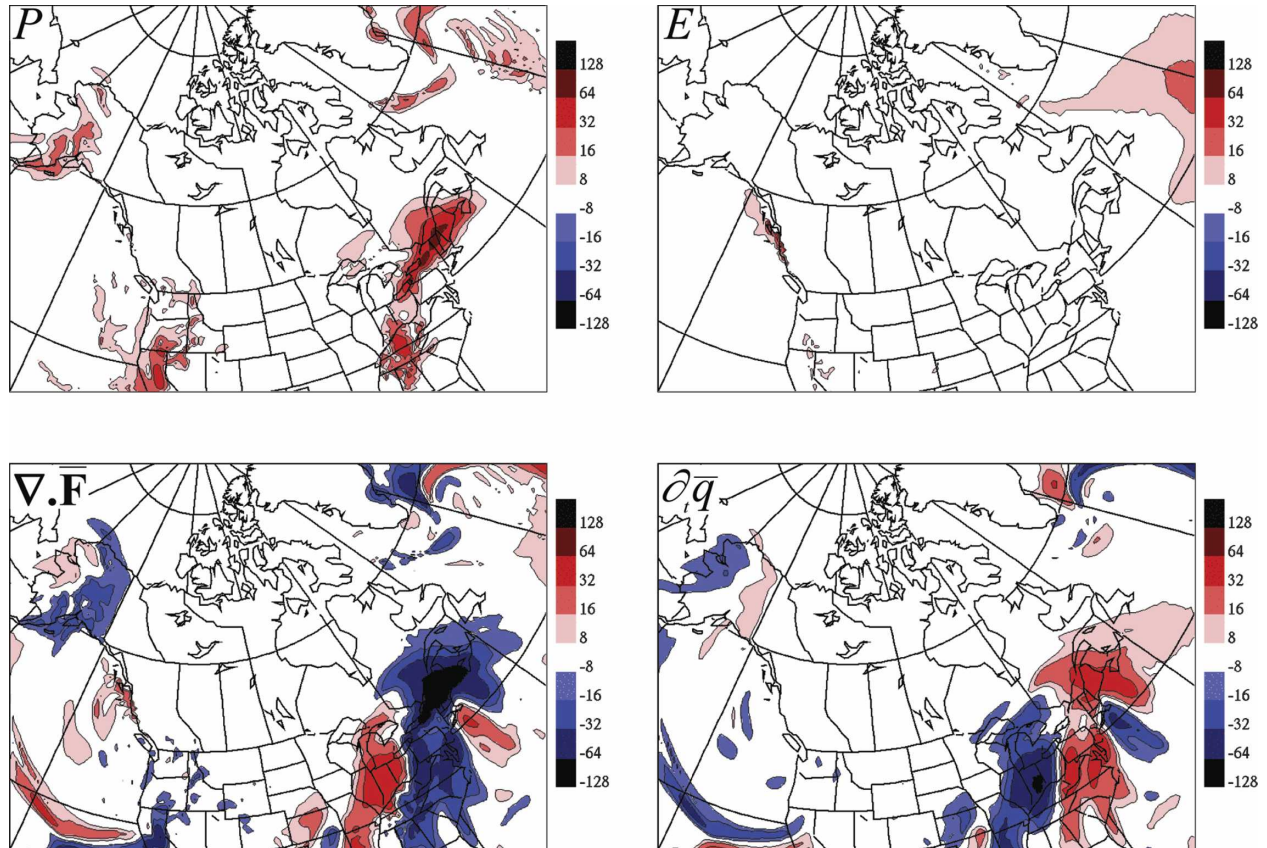


FIG. 5. Water vapor budget terms calculated from the CRCM simulation for 15 Feb 1990. Here P is the 6-h mean precipitation rate, E is the evapotranspiration rate, $\nabla \cdot \mathbf{F}$ is the divergence of the vertically integrated moisture flux, and $\partial \bar{q}$ is the vertically integrated water vapor tendency. The divergence was calculated on Gal-Chen levels during the CRCM integration. Here P , E , and \mathbf{F} were cumulated over 6 h from 0600 to 1200 UTC. Here $\partial \bar{q}$ is evaluated as the difference between values at 1200 and values at 0600 UTC. Values are in mm day^{-1} .

outbreak over the ocean at this specific time; this term is the weakest term of the budget. Indeed, the 6-h mean divergence of the moisture flux is nearly balanced by the precipitation and the tendency of the water vapor. The balance of the water budget will be rather different when considering a longer time average as will be shown later.

The scale decomposition will be first applied to this specific time to gain insight into the contributions of various scales before pursuing the study on a monthly time scale.

2) DIVERGENCE OF THE MOISTURE FLUX

Figure 6 displays the nine moisture flux divergence terms resulting from the scale decomposition of the wind and moisture. The term $\nabla \cdot \mathbf{V}_0 q_0 = \mathbf{V}_0 q_0 \cdot \nabla \beta$ actually represents the gradient of the mask β , as \mathbf{V}_0 and q_0 are constant values; it is not giving much information and it is very small. The dominant terms of this decom-

position are those involving the large-scale humidity q_L interacting with the large and the very large scale flow ($\nabla \cdot \mathbf{V}_0 q_L$ and $\nabla \cdot \mathbf{V}_L q_L$): it is noteworthy that these two terms have opposite signs for the band off the west coast, whereas they tend to have the same sign for the dipole along the east coast. The dominant small-scale terms are those related to the small-scale humidity interacting with large-scale winds and vice versa ($\nabla \cdot \mathbf{V}_S q_L$ and $\nabla \cdot \mathbf{V}_L q_S$): these two terms tend to modulate the large-scale structures that are represented in the large-scale terms, such as to increase the central amplitude and to sharpen the spatial structure by decreasing their spatial extension. The term $\nabla \cdot \mathbf{V}_S q_L$ has maximum values over the Appalachian Mountains with a strong topographic forcing on the small-scale wind, whereas the term $\nabla \cdot \mathbf{V}_L q_S$ shows small scales over both the ocean and the continent where the humidity field exhibit small scales. The term involving only small scales $\nabla \cdot \mathbf{V}_S q_S$ is weak but still shows an interesting

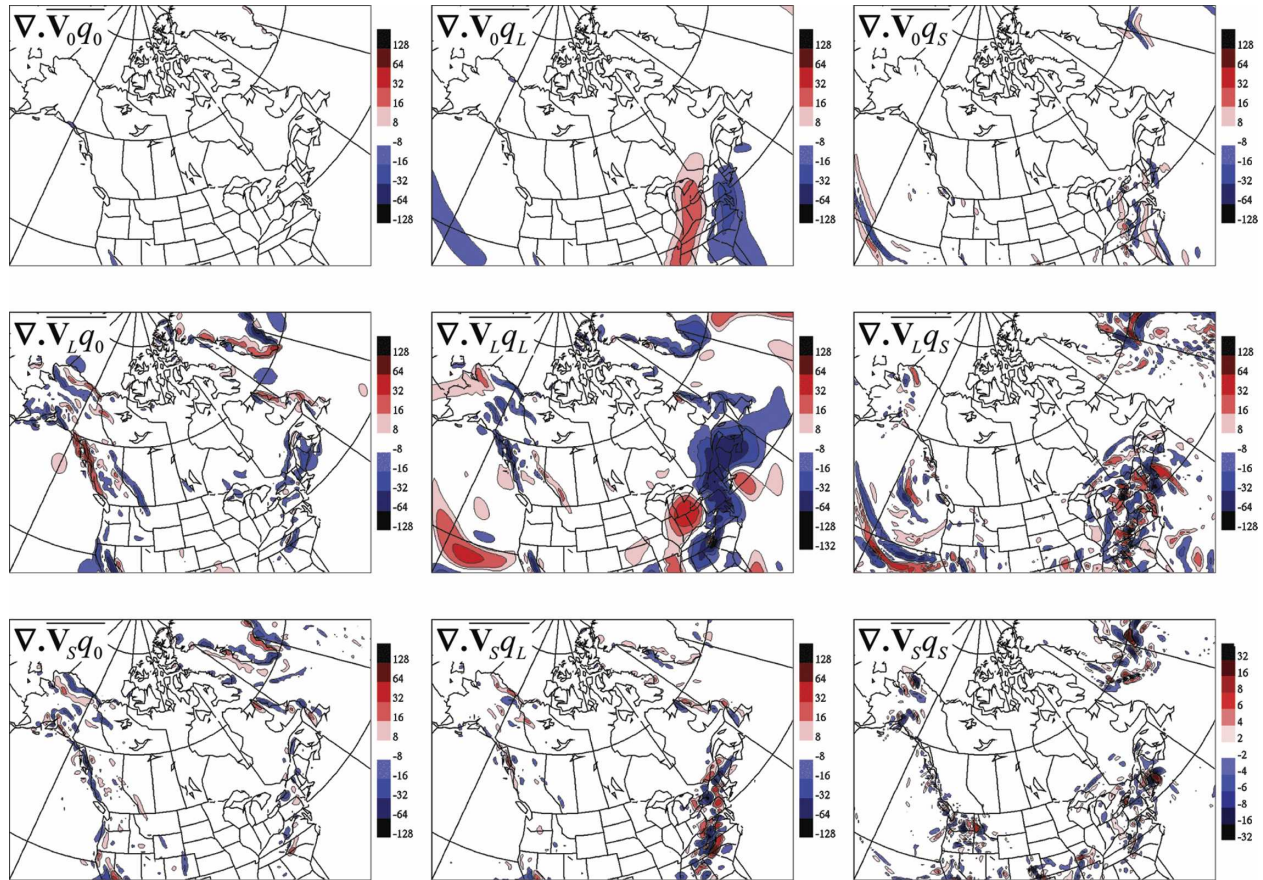


FIG. 6. Scale decomposition of the divergence of the vertically integrated moisture flux into nine components—instantaneous at 1200 UTC on 15 Feb 1990. The subscript 0 represents the very large scales not resolved by CRCM, the subscript L represents large scales that are both resolved by CRCM and NCEP (scales larger than 1000 km) and the subscript S represents small scales that are only resolved by CRCM (scales smaller than 600 km). Note the different scale used for $\nabla \cdot \nabla_s q_s$.

signal; this term shows greater activity of small scales over the continent than over the ocean.

For comparison, the same decomposition is applied to the NCEP driving data (Fig. 7). Results show that the cross terms that involve small scales that are not resolved in NCEP data have almost no contribution, as expected. If one looks carefully, some weak features are present over the east coast, but these are errors that can be attributed either to the fact that the CRCM topography is used to compute the β term, but also because of residual errors due to interpolations and due to the cosine transform, which appear especially in the small-scale humidity term q_s . The large-scale behavior of the NCEP–NCAR reanalyses is similar to that of the CRCM simulation, also to be expected given that these reanalyses were providing the boundary conditions. The terms involving q_0 are slightly stronger in the NCEP–NCAR reanalyses data than in the CRCM output, because the CRCM is slightly underestimating the average humidity at this particular time (1.8 g kg^{-1} for

MRCC versus 2.0 g kg^{-1} for NCEP at 850 hPa). The spatial average of the wind speed is about the same at 850 hPa (4.4 m s^{-1} or MRCC versus 4.25 for NCEP) and the direction is almost identical, too.

3) SCALE DECOMPOSITION OF E , P , AND $\partial_t q$

Figure 8 shows the precipitation rate, the evapotranspiration, and the water vapor tendency, as well as their decomposition into their large and small scales between 6 and 12 UTC for 15 February 1990. The 0 term is not shown, as it is constant. The precipitation field has two main large-scale bands of precipitation over the west and east coasts, and the small scales are confined over the same regions, mainly over topographic features. The evapotranspiration for this time presents only a large-scale structure and essentially no small scales. The tendency of water vapor shows two large-scale structures associated with the two bands of precipitation, and the small scales are present over the ocean off the west coast; some small scales in the water vapor

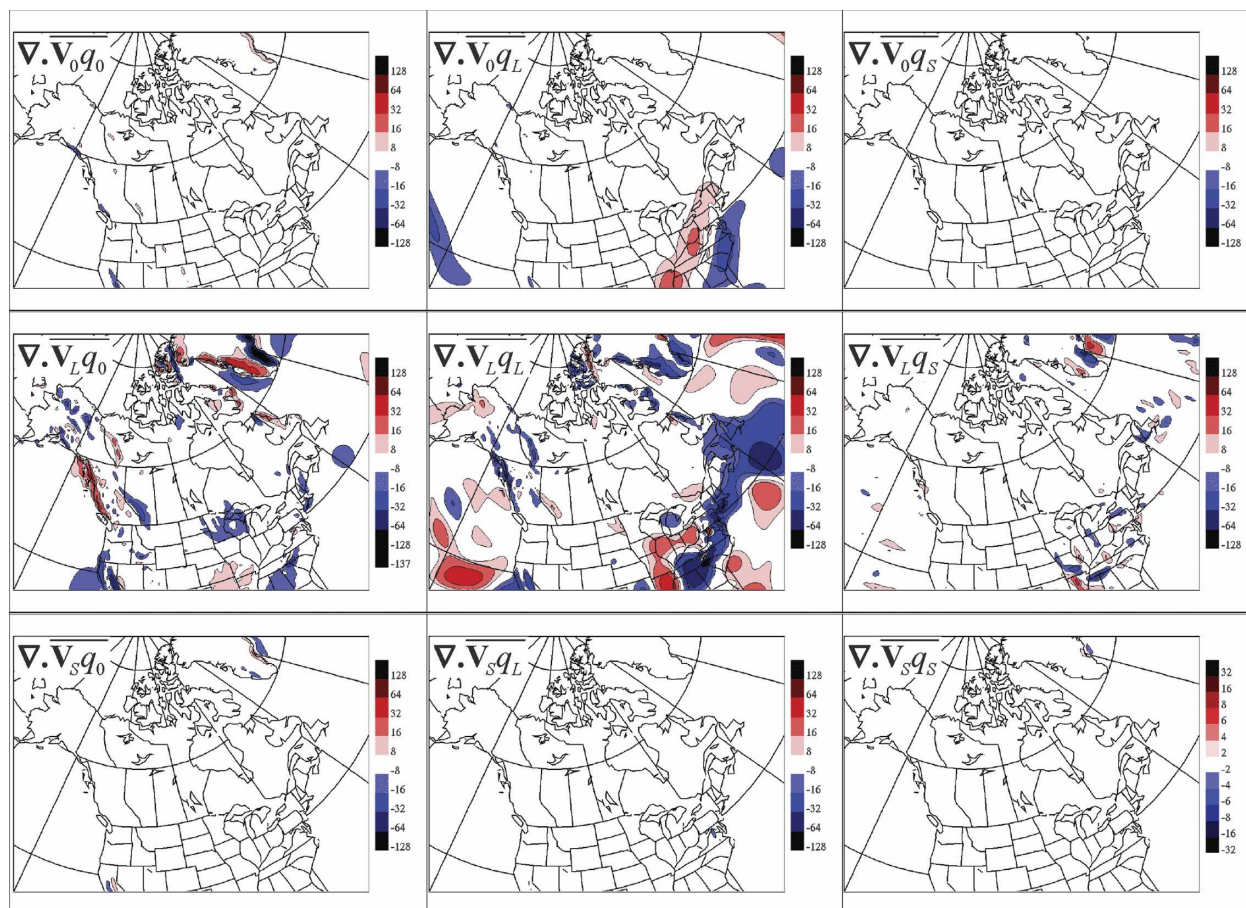


FIG. 7. Same as in Fig. 6 but for the NCEP-NCAR reanalysis data.

tendency seem to be forced by the topography for this time over the Appalachians.

b. Monthly mean statistics

1) DIVERGENCE OF THE MOISTURE FLUX

In this section, the monthly mean budget of February 1990 is analyzed. Figure 9 shows the four terms of the water budget for the monthly mean, evaluated as time cumulations of time step values in Gal-Chen coordinate. Because the monthly mean atmospheric moisture tendency is very small, the main balance is now between the divergence of moisture flux and evaporation minus precipitation ($E - P$). Two main precipitation regions are dominating this winter month, one over the west coast of North America and the second over the east coast of North America. For comparison, the precipitation produced as part of the NCEP-NCAR reanalysis system and by analysis of observations by C. J. Willmott and K. Matsuura (2001, personal communication; version of July 2001 available online at <http://climate.geog.udel.edu/~climate/>) are shown in Fig. 10.

Both the CRCM simulation and the NCEP-NCAR reanalyses tend to produce too much precipitation over the coastal regions and the Rocky Mountains, whereas they tend to produce too little precipitation over the Appalachian Mountains for this month. Nevertheless they both capture the two main regions of precipitation.

The February 1990 time-mean vertically integrated divergence of the moisture flux $\nabla \cdot [\bar{\mathbf{V}}q]$ is decomposed into its divergence due to stationary eddies (divergence calculated from the monthly mean wind and monthly mean humidity fields, $\nabla \cdot [\bar{\mathbf{V}}][\bar{q}]$), and its divergence due to transient eddies (divergence calculated from the covariance of the temporal deviations from the monthly mean wind and the monthly mean humidity, $\nabla \cdot [\mathbf{V}'q']$) and displayed in Fig. 11. These fluxes are evaluated from time samples of model data interpolated on pressure levels. The time fluctuation TF is also shown. On the east coast, the time-mean divergence is dominated by the transient eddy contribution. There the divergence due to stationary eddies is of opposite sign and tends to partly cancel the divergence due to transient eddies. It is not clear why. By looking at the mean wind

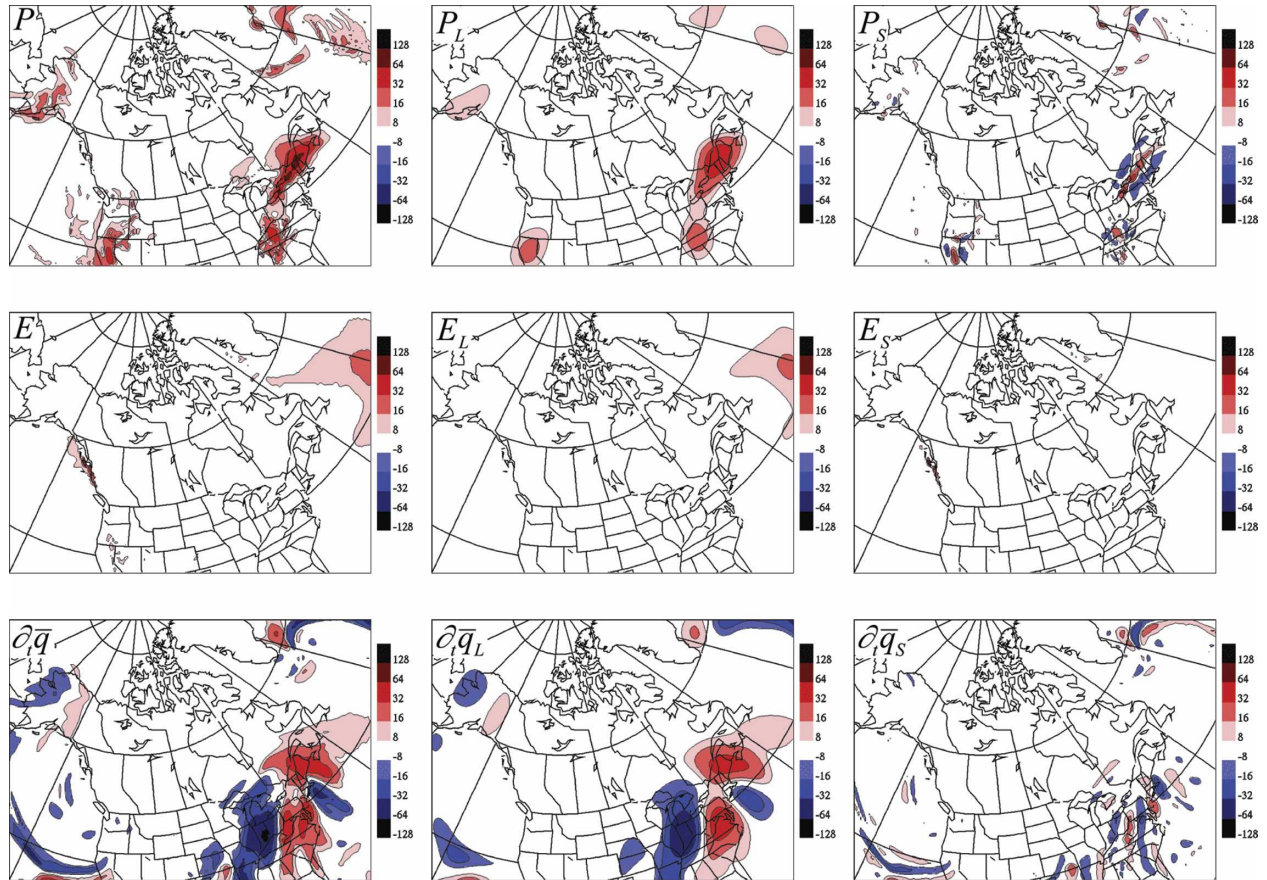


FIG. 8. The CRCM-simulated fields at 15 Feb 1990 between 0600 and 1200 UTC for the (top) precipitation, (middle) evapotranspiration, and (bottom) water vapor tendency. (left column) Total fields and their decomposition into (middle column) large (larger than 1000 km) and (right column) small (smaller than 600 km) scales.

and mean humidity fields (not shown), one can see that the region of divergence due to the stationary eddies on the east coast results mainly from a divergent wind acting on a relatively constant humidity, whereas the region of convergence is due to a gradient of humidity, with relatively constant wind. On the west coast on the other hand, the time-mean divergence is more a combination of the two components, the stationary and the transient eddy contributions are reinforcing one another to compose the time-mean convergence.

Figures 12 and 13 are showing the transient and the stationary eddy components, respectively, decomposed into the nine terms. They have very different contributions. The transient eddy component (Fig. 12) is dominated by the term involving large-scale wind and large-scale humidity; all the other terms are negligible. The equivalent term $\nabla \cdot [\mathbf{V}'_L q'_L]$ calculated from NCEP data (not shown) is very similar, with a correlation coefficient of 0.89 with the CRCM-simulated results. Interactions between large- and small-scale terms have a small contribution to the total divergence, mainly

through the term $\nabla \cdot [\mathbf{V}'_L q'_S]$; the self-interaction of small scales is very weak. The divergence of the moisture flux due to the stationary eddies is quite different (Fig. 13). All the terms involving large and very large scales play an important role in contributing to the total divergence. These terms seem to be dominated by topographic features with strong values near main mountains. The nonlinear interaction terms involving $[\mathbf{V}_S]$ and/or $[q_S]$ that represent the added value are all showing a nonnegligible contribution and seem to be, similarly to the large-scale terms, dominated by topographic forcing. The spatial correlation between CRCM and NCEP is high with values of 0.82, 0.86, and 0.92 for the terms $\nabla \cdot [\mathbf{V}_L][q_L]$, $\nabla \cdot [\mathbf{V}_L][q_0]$, and $\nabla \cdot [\mathbf{V}_0][q_L]$, respectively.

2) TIME FLUCTUATION OF THE MOISTURE FLUX DIVERGENCE

In this section, we examine the standard deviation of the time fluctuation of the vertically integrated divergence (TF) for the month of February 1990 (lower-left

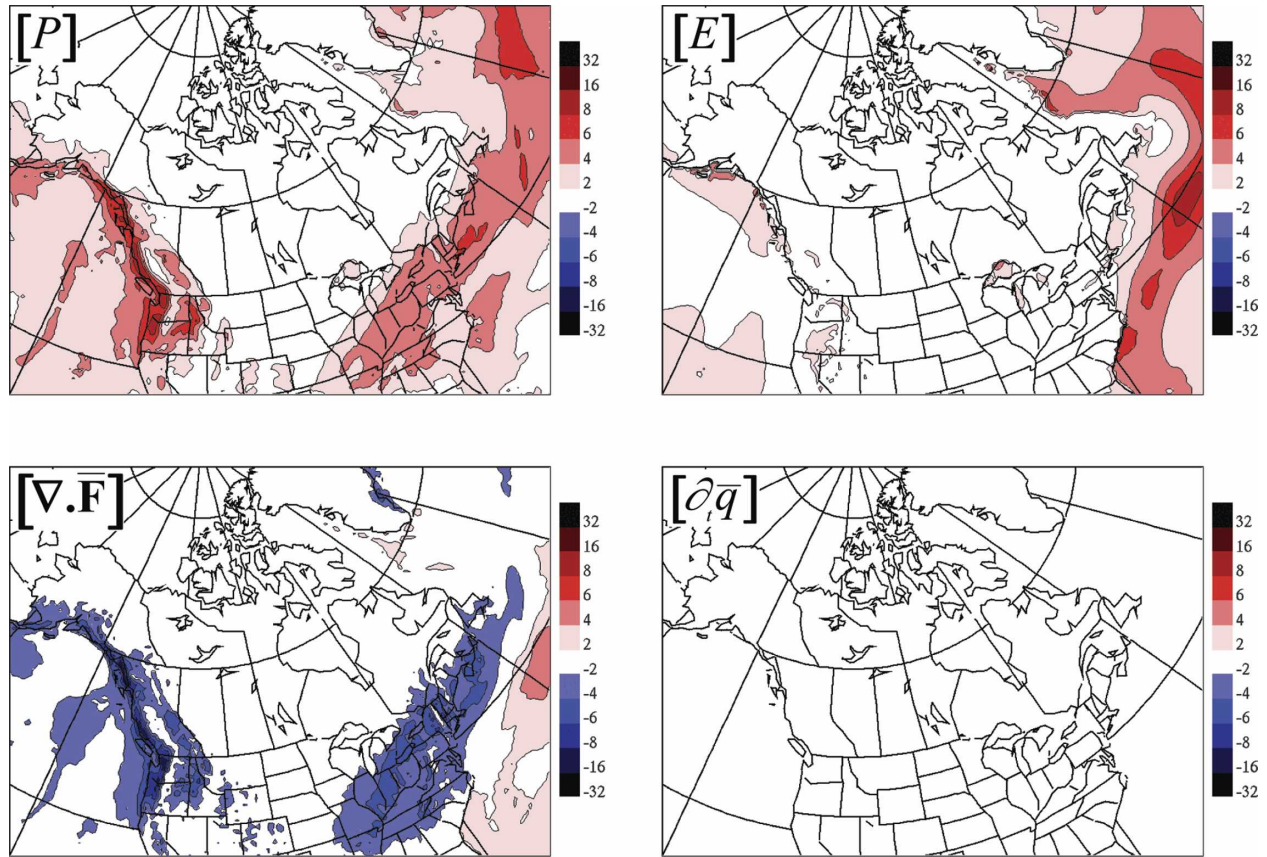


FIG. 9. Monthly mean water vapor budget terms calculated from the CRCM simulation for the month of February 1990. Here $[P]$ is the mean precipitation rate, $[E]$ is the mean evapotranspiration rate, $[\nabla \cdot \bar{F}]$ is the mean divergence of the vertically integrated moisture flux in the Gal-Chen coordinate, and $[\partial \bar{q}]$ is the mean water vapor tendency. All these fields are evaluated as time cumulative.

panel in Fig. 11). By contrast to the time mean (upper-left panel in Fig. 11), TF is maximum over the Pacific and the Atlantic Oceans instead of over the continent. If we examine TF of the nine decomposed terms (Fig. 14), the two dominant large-scale terms are the same as

the ones for the instantaneous decomposition for 15 February 1990 (Fig. 6), which are the terms involving the large-scale humidity and the large and very large scale wind (TF_{OL} and TF_{LL}). The correlation coefficients between CRCM and NCEP for TF_{LL} , TF_{OL} , and

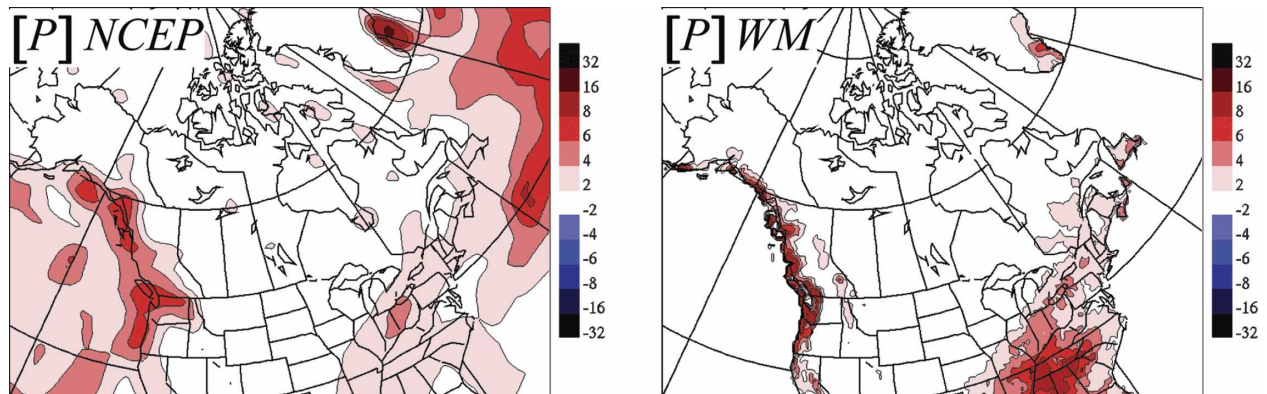


FIG. 10. Monthly mean precipitation produced by NCEP-NCAR reanalyses (P NCEP) and from analysis of observations over the continent by C. J. Willmott and K. Matsuura (2001, personal communication; P WM) for February 1990.

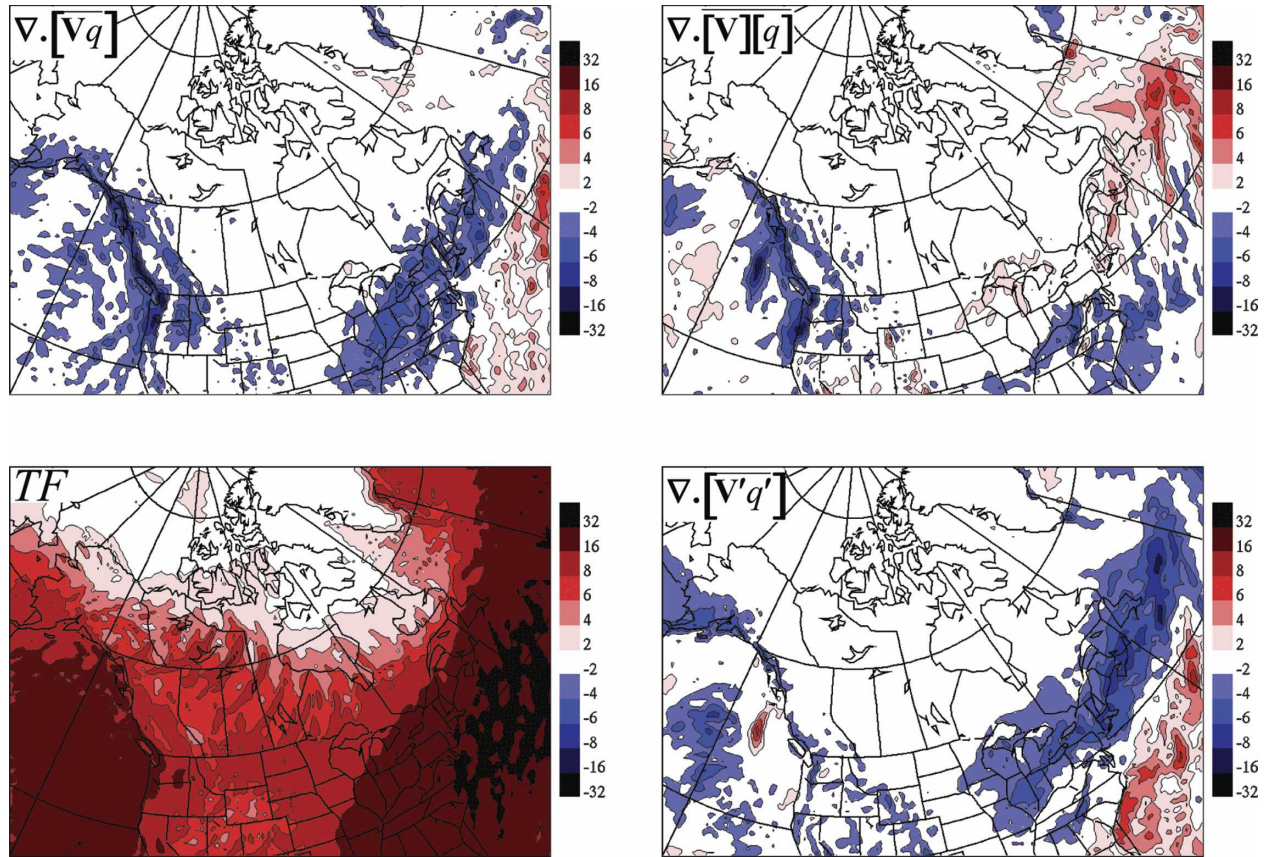


FIG. 11. Decomposition of the time-mean divergence of the moisture flux $\nabla \cdot [\nabla q]$ into its component due to stationary eddies $\nabla \cdot [\mathbf{V}][q]$ and its component due to transient eddies $\nabla \cdot [\mathbf{V}'q']$, and the standard deviation of the time fluctuation of the divergence of moisture flux (TF) for the month of February 1990.

TF_{L0} are very high with values of 0.97, 0.98, and 0.92, respectively. The nonlinear terms involving the small-scale humidity (TF_{0S} and TF_{LS}) are strong over the oceans and tend to show bandlike structures for these monthly statistics. The nonlinear terms involving small-scale wind (TF_{S0} and TF_{SL}) have stronger values inland near major mountainous regions. The contribution from the small-scale wind (TF_{SX}) tends to have amplitude mainly over topographic features, whereas the contribution from the humidity field (TF_{XS}) has amplitude mainly over the ocean associated with the passage of weather disturbances. The topographic features appear to create small-scale wind that will then transport the large-scale humidity and contribute substantially to the moisture flux divergence. The small-scale self-interaction term (TF_{SS}) is weak but still shows some small-scale contribution near the Rocky and the Appalachian Mountains and over the Atlantic Ocean where frequent weather disturbances are passing in winter-time. Although TF does not contribute to the monthly mean precipitation generation, it is part of the internal

variability in the atmosphere, and hence can be contributing to extreme events.

4. Discussion

In this section we will first evaluate the impact of vertical interpolation and time sampling on the reliability of the water budget; then we will compare some of our results with those of van Tuyl and Errico (1989). As a result of the vertical interpolation from model Gal-Chen to pressure coordinates, the budget terms are subject to errors. Moreover, the moisture flux on pressure levels is calculated using instantaneous 6-h output, whereas the model moisture flux calculated on Gal-Chen levels is aggregated in time over the archival interval; time truncation constitutes another source of error to the pressure-coordinate budget terms. The combined effect of these two sources of errors can be seen by comparing the vertically integrated time-mean flux in the lower-left panel in Fig. 9 (Gal-Chen, time aggregated) and the upper-left panel in Fig. 11 (pressure,

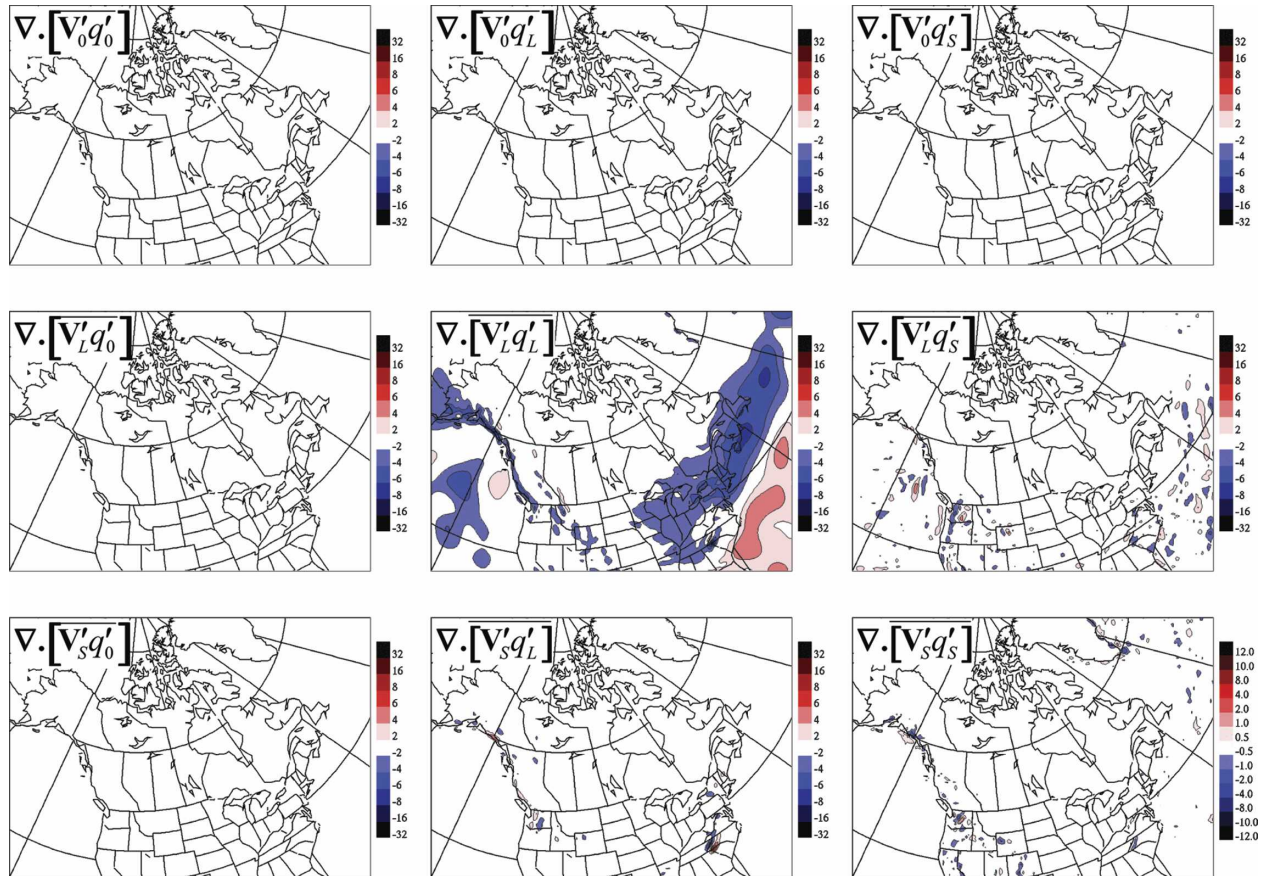


FIG. 12. Same as in Fig. 6 but for the divergence of the moisture flux due to transient eddies for the month of February 1990.

time sampled). To estimate the relative contributions to these errors, an extra simulation has been performed for the month of February 1990 with output archived every time step (i.e., every 15 min). In addition, output data have been interpolated into two different sets of pressure levels: first into the 17 pressure levels of the NCEP–NCAR reanalyses, and second to a set of 30 pressure levels used for the final results. In this section the vertically integrated divergence of the moisture flux is examined to show the effects of the 6-h time sampling and vertical interpolation. Even though it would be nice to save data on Gal-Chen levels for a better accuracy of the vertically integrated moisture flux; it would not be advisable to do the scale decomposition on Gal-Chen levels especially in mountainous regions.

Spatial correlations of monthly mean vertically integrated moisture flux divergence and $E - P$ are first used to estimate the errors associated with vertical interpolation and time sampling. Six different estimates of the time-mean vertically integrated moisture divergence are intercompared: one calculated on Gal-Chen levels during integration of the model with aggregation

over 6 h (GC6), one calculated on Gal-Chen levels with output every 15 min (GC15), two estimates calculated on 17 and 30 pressure levels, respectively, using instantaneous 6-h samples (P17-6 and P30-6), and two estimates calculated on 17 and 30 pressure levels, respectively, every 15 min (P17-15 and P30-15; see Table 1 for a summary of these six estimates). The spatial correlations between monthly mean divergences calculated on Gal-Chen levels and divergences calculated on pressure levels are all above 0.83, which is quite good (Table 2). The correlation between pressure estimates and Gal-Chen values increases when using 30 pressure levels instead of 17; for example, the correlation between GC15 and P17-15 is 0.89, whereas the correlation between GC15 and P30-15 is 0.98. The same increase of correlation is seen for the 6-h archival period, with a correlation of 0.83 between GC6 and P17-6 increasing to 0.91 between GC6 and P30-6. It is thus important to have a good vertical resolution in the low levels when interpolating data from Gal-Chen to pressure levels to capture the layers where atmospheric moisture is concentrated and where the winds vary rapidly. As for the

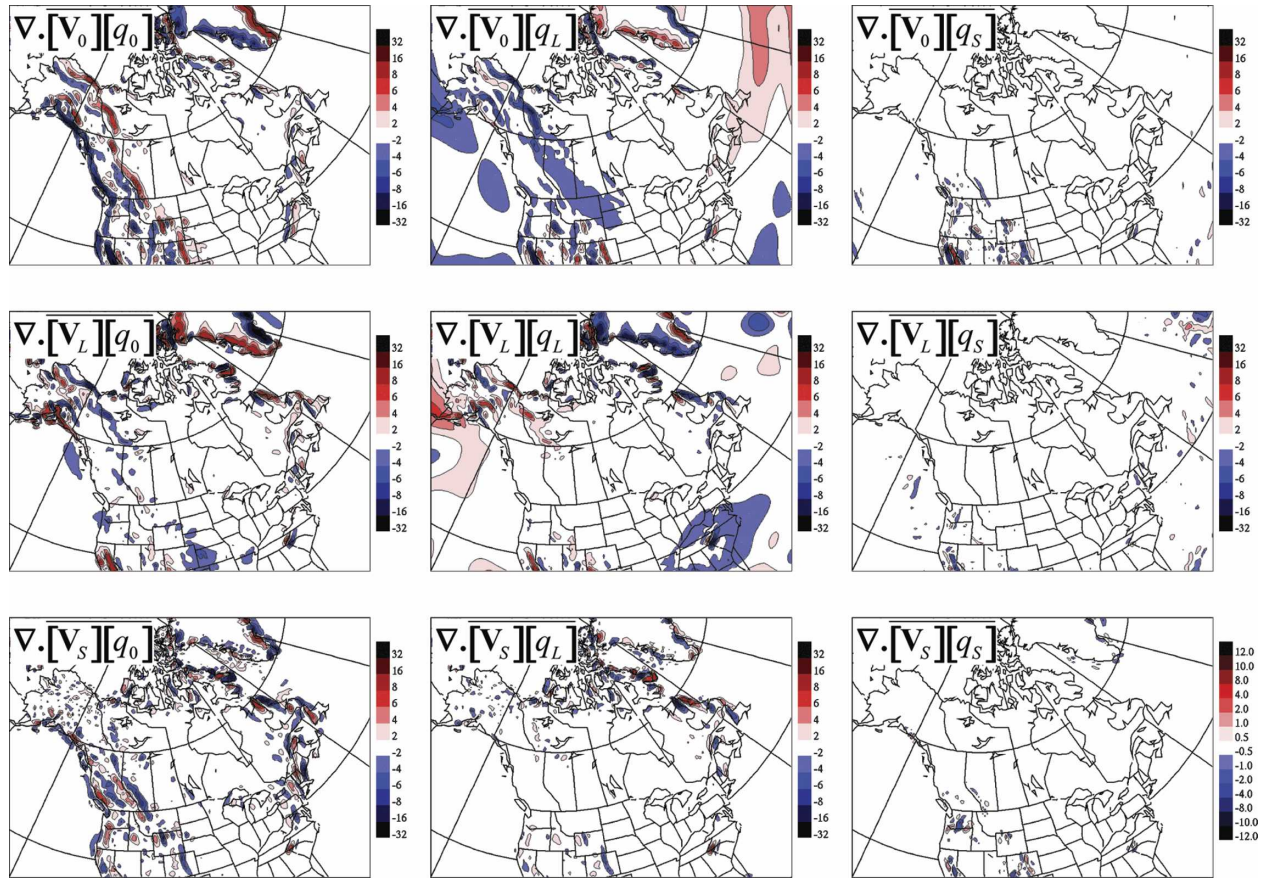


FIG. 13. Same as in Fig. 6 but for the divergence of the moisture flux due to the stationary eddies for the month of February 1990.

temporal resolution, the sampling of the data over 6 h instead of using data at every time step decreases the spatial correlation from 0.98 to 0.91 and from 0.89 to 0.83, depending on the number of pressure levels considered. The spatial correlation between any divergence estimates with $E - P$ is quite good, with values above 0.87; the best results (correlation = 0.97) are of course obtained with calculations made at time step interval (15 min) using data in model coordinates (GC).

Variance spectra of the six divergence estimates for the time-mean part (defined as the spectra of the monthly mean, $||\nabla \cdot \bar{\mathbf{F}}(k)||^2$, with k as the modulus of the two-dimensional wavenumber) and the time-fluctuation part (defined as the monthly mean spectra minus spectra of the monthly mean, $||(\nabla \cdot \bar{\mathbf{F}})'(k)||^2 = ||\nabla \cdot \bar{\mathbf{F}}(k)||^2 - ||\nabla \cdot \bar{\mathbf{F}}(k)||^2$) are displayed in Fig. 15. All estimates agree fairly well for scales larger than 2000 km. It is worth noting that the time-fluctuation part has much more variance than the time-mean part.

The spectra for the time-fluctuation part of the divergence estimate GC6 shows noticeably smaller variance than the divergence estimate GC15 for scales

shorter than 1000 km; the difference reflects the part of the variance associated with time scales between 1/2 and 12 h, which is lost by time aggregation in GC6. The time-fluctuation spectra calculated in pressure coordinates are fairly close to GC15: the green line (P17-15) is hidden by the red line (P17-6), and the cyan (P30-15) and purple (P30-6) lines are hidden by the yellow line (GC15), as the spectra are almost identical, meaning that the impact of the time sampling on the time-fluctuation part is negligible. The approximation due to vertical interpolation (yellow line versus red line) affects the scales smaller than 300 km, and by using coarse vertical resolution, the spectra tends to have somewhat excessive variance for these scales.

The analysis of the impact of temporal and vertical resolution on the spectra of the moisture flux divergence for the time-mean part is more complex. The divergence of the time-mean vertically integrated moisture flux should compare to $E - P$. A difference between GC15 and $E - P$ 15 is present for small scales (scales less than 200 km) with a bump in the spectra of cumulated divergence around the 150-km wavelength.

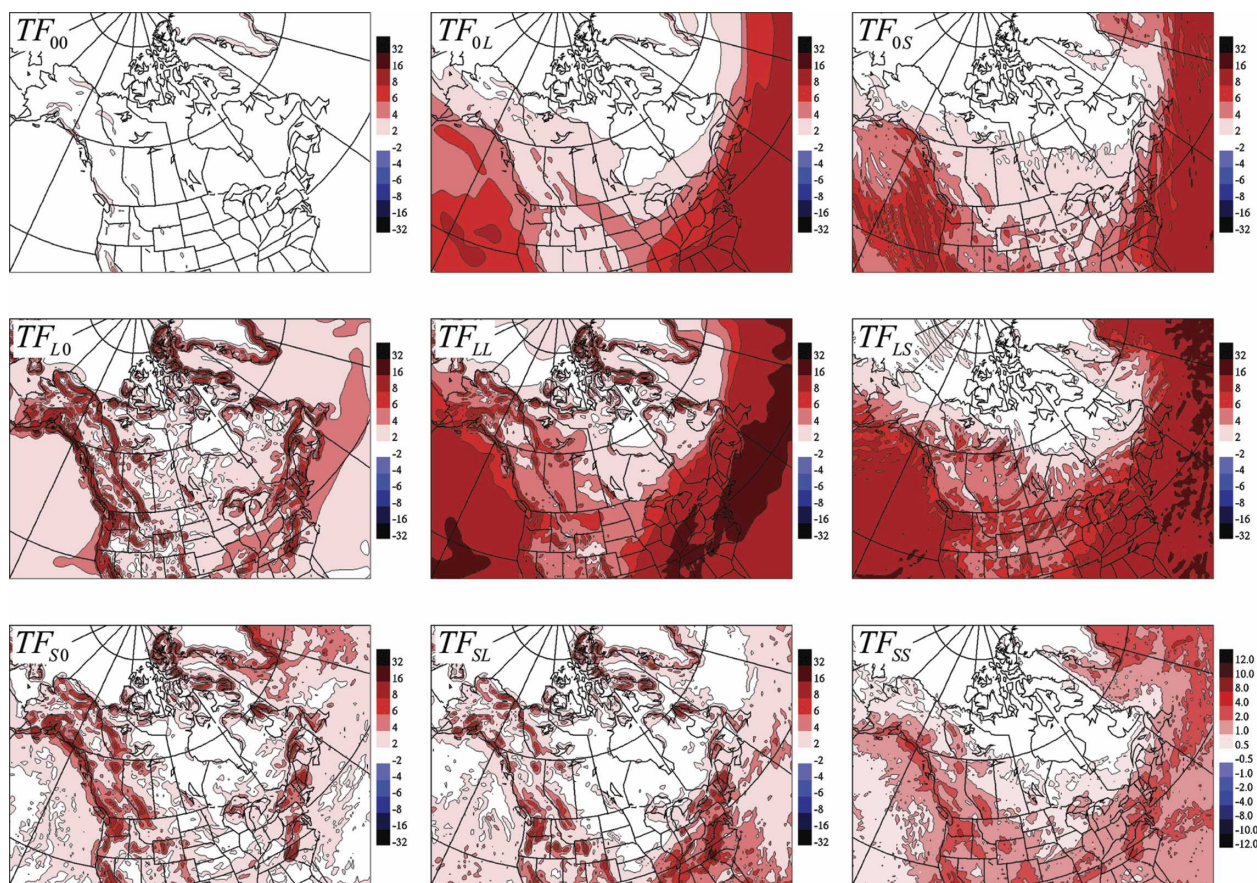


FIG. 14. Same as in Fig. 6 but for the standard deviation of the time fluctuation of the divergence of the vertically integrated moisture flux for the month of February 1990. Note the different scale used for TF_{SS} .

This bump is likely the result of our use of a centered finite-difference Eulerian discretization to estimate the divergence diagnostically while the CRCM used a semi-Lagrangian transport scheme that is known to be dissipative for the short scales due to the cubic interpolations. But it must be kept in mind that the time-mean part is at least one order of magnitude smaller than the time-fluctuation dominant part, thus it makes little difference to the total divergence in practice. A 6-h time sampling compared to 15 min tends to slightly increase

the variance of medium to small scales (scales between about 600 and 200 km). A coarse vertical resolution on pressure levels in the low levels (P17-15 versus P30-15) artificially adds power to the medium- and small-scale spectra (scales smaller than 600 km).

The monthly mean vertically integrated divergence of moisture flux calculated on 17 and 30 pressure levels with 6-h and 15-min time-sampling intervals are dis-

TABLE 1. Summary of the different estimations of the moisture flux divergence.

Name	Vertical levels	Time resolution
GC6	Gal-Chen: 29 levels	Cumulation 6 h
GC15	Gal-Chen: 29 levels	15 min
P17-6	Pressure: 17 levels	Sampled 6 h
P17-15	Pressure: 17 levels	15 min
P30-6	Pressure: 30 levels	Sampled 6 h
P30-15	Pressure: 30 levels	15 min

TABLE 2. Spatial correlation coefficients for the monthly averaged fields (i.e., the stationary part).

Field 1	Field 2	Spatial correlation between fields 1 and 2
Divergence GC15	Divergence P30-15	0.98
Divergence GC15	Divergence P17-15	0.89
Divergence GC6	Divergence P30-6	0.91
Divergence GC6	Divergence P17-6	0.83
$E - P$ 15	Divergence GC15	0.97
$E - P$ 15	Divergence P30-15	0.96
$E - P$ 6	Divergence P30-6	0.87

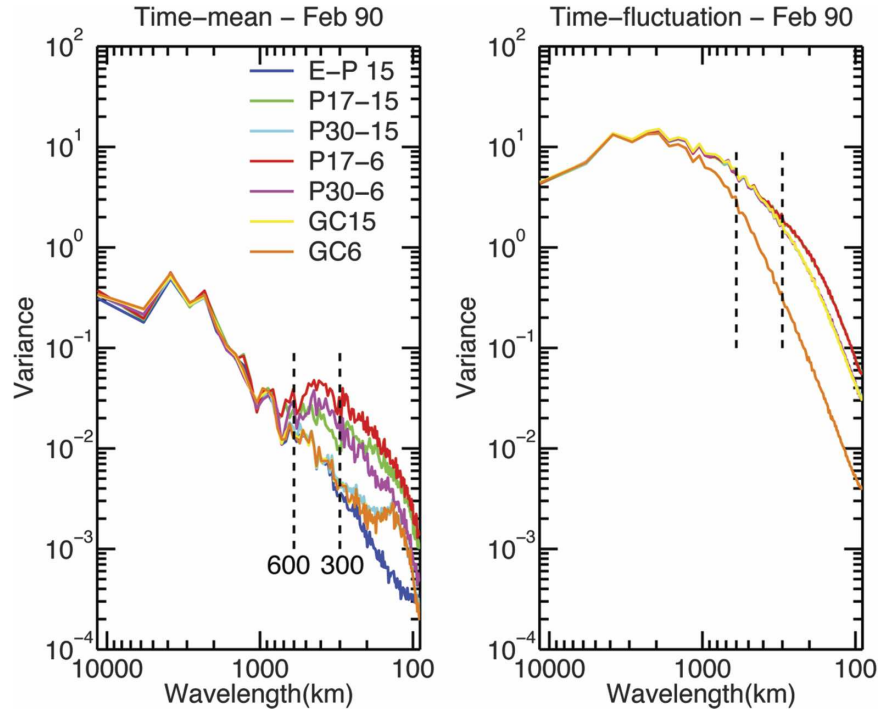


FIG. 15. Variance spectra of the divergence of the vertically integrated moisture flux calculated over the Gal-Chen levels (GC6 and GC15) and calculated over pressure levels (P17-6, P17-15, P30-6, and P30-15) compared to the variance spectra of $E - P$ 15 (calculated with 15-min intervals). (left) Time-mean part of the divergence $[(\nabla \cdot \bar{\mathbf{F}})(k)]^2$; (right) time-fluctuation part $[(\nabla \cdot \mathbf{F}')(k)]^2$. For the time-fluctuation part, the cyan (P30-15) and the purple (P30-6) lines are hidden by the yellow line (GC15), and the green line (P17-15) is hidden by the red line (P17-6) because they are almost identical.

played in Fig. 16. The major difference between P17 and P30 is near-topographic features where much more noise appears when using only 17 pressure levels for the computation of the divergence of moisture flux. The correlation between NCEP and CRCM for the large-scale terms (0 and L) is not improved when using 30 levels of pressure instead of 17, meaning that the increased pressure resolution in the low levels mainly affects the small scales that represent the added value of the CRCM. The divergence calculated on pressure levels is noisier when using 6-h time sampling. Comparing with the divergence computed on Gal-Chen levels (Fig. 9), it can be seen that P30-15 and GC15 are almost identical as was noted also for their spectra (Fig. 15). The noise seen for P30-6 is due to the 6-h sampling resulting in using 24 times less data to calculate the monthly average compared to P30-15.

Figure 17 shows the rapid degradation of the moisture flux divergence due to an increase of output interval from 1 time step (15 min) to 12 time steps (3 h). This figure was done using 30 pressure levels. With a 3 time step output, the contours of the major divergence-

convergence features start to blur. As the sampling interval is lengthened, it is becoming more and more blurred and, when using a 12 time step interval, noise begins to appear where there should not be any divergence or convergence (e.g., over the Pacific and the Atlantic Oceans). With a 24 time step interval (6 h), it is even more pronounced (P30-6; Fig. 16 lower-left panel).

Comparing our results with those of the study by van Tuyl and Errico (1989), we found, as they did, that the topographic forcing was a dominant small-scale forcing for the stationary part of the divergence of the moisture flux over the continent and especially topographic forcing on the wind. The topographic features appear to induce small-scale winds that transport the large-scale moisture and contribute substantially to the moisture flux divergence. The small-scale humidity field, by contrast, showed both topographic and oceanic forcings, and the time-fluctuation part of the moisture flux divergence does not show a dominant topographic forcing. According to the study of van Tuyl and Errico, the self-interactions of small scales do not contribute to

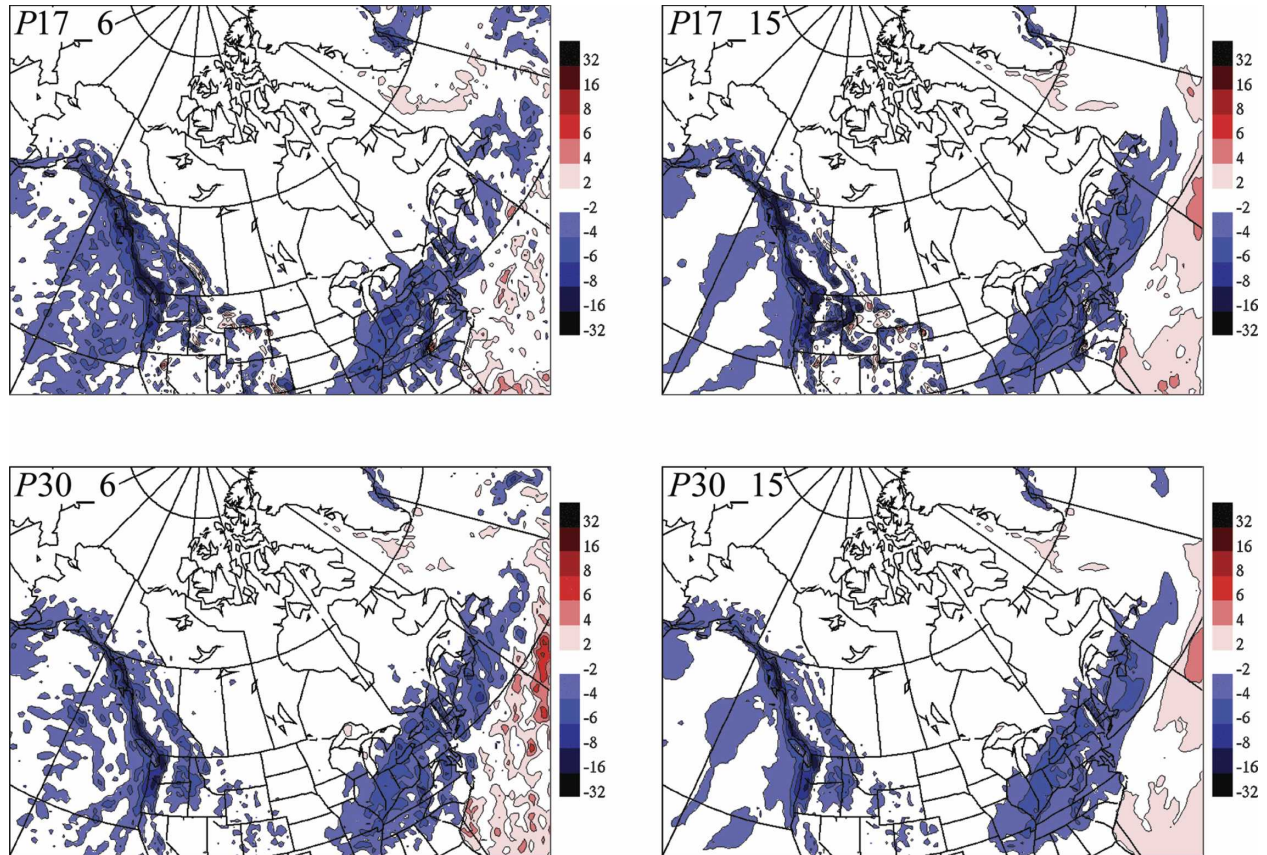


FIG. 16. Monthly mean (February 1990) divergence of the moisture flux calculated over 17 pressure levels, P17-6 and P17-15 for 6-h output and for 15-min output (every time step), respectively, and calculated over 30 pressure levels, P30-6 and P30-15, for 6-h and 15-min output, respectively. It is to be compared to the divergence of the moisture flux calculated over the Gal-Chen levels (Fig. 8). The pressure calculation used 6-h samples whereas the computation over the Gal-Chen levels is an aggregation of the time step data over 6 h.

large scales; this point is difficult to assess in our study because self-interactions of small scales are very weak. Figure 18 shows, for two of the nine moisture flux divergence terms (namely, $\nabla \cdot [\mathbf{V}_0][q_L]$ and $\nabla \cdot [\mathbf{V}_0][q_S]$), their projection into large and small scales. This decomposition reveals that interaction between large and small scales creates predominantly small scales (the same result is obtained when considering any quadratic terms involving large or very large scales interacting with small scales). Self-interaction of large or very large scales creates both large and small scales that are comparable to the small scales created by the interaction of small and large scales (again the same result is obtained when using any combination of large and very large terms). These results are at variance with those of van Tuyl and Errico since they did not see any significant interactions between large and small scales. As far as we can see using only three bands, the moisture variance tends to cascade downscale, but too few wave-

bands are used in our study to address this issue properly.

5. Conclusions and future work

The CRCM reproduces the large-scale structures of the NCEP-NCAR reanalyses used to drive the simulation and the dominant large-scale term is the synoptic term (scales between 1000 km and about 6000 km). The added value produced by the CRCM is dominantly represented by nonlinear interactions between small- and large-scale features in this case. The dominant small-scale forcing of the wind is the topography as seen by the term $\nabla \cdot \overline{\mathbf{V}_S q_L}$ and it is transporting the large-scale humidity, whereas there is both topographic and oceanic small-scale forcing on the humidity field that is transported by large-scale wind (term $\nabla \cdot \overline{\mathbf{V}_L q_S}$).

The vertically integrated divergence of the moisture flux due to transient eddies for one winter month is

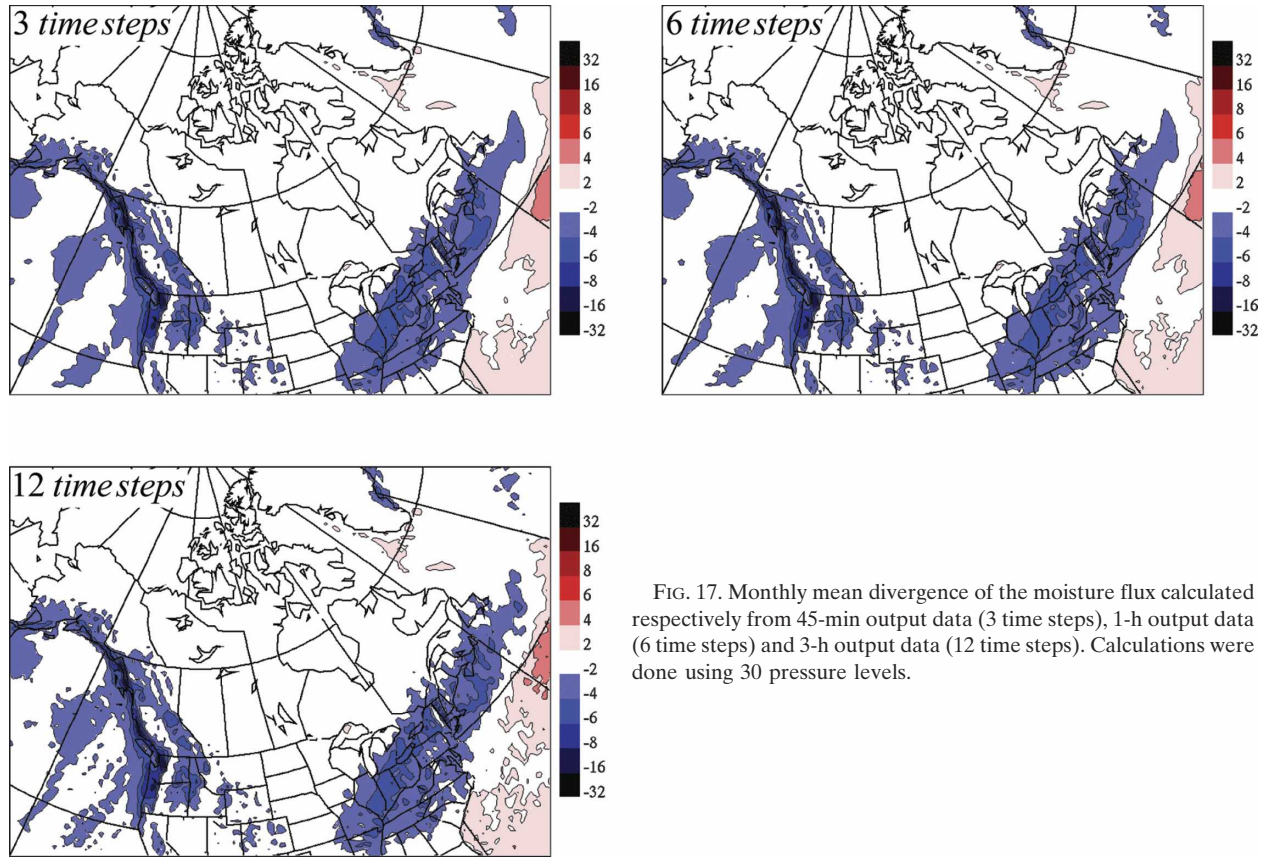


FIG. 17. Monthly mean divergence of the moisture flux calculated respectively from 45-min output data (3 time steps), 1-h output data (6 time steps) and 3-h output data (12 time steps). Calculations were done using 30 pressure levels.

dominated by synoptic scales with negligible contribution from small scales, whereas the divergence due to stationary eddies presents substantial added value through the nonlinear interactions between the small and the large scales over the continent. The main forcing tends to be topographic, which is a stationary forcing, this is the reason why the small scales are dominantly contributing to the part due the stationary eddies. Finally, the large scales simulated by the CRCM are quite similar compared to the large scales present in the NCEP–NCAR reanalyses for both the stationary and transient eddy components; both the stationary and transient eddy component are of equivalent magnitude.

The time fluctuation of the vertically integrated moisture flux divergence (TF) for the month of February 1990 is maximum over the oceans for both the large- and small-scale terms. The dominant large-scale terms are those involving the large-scale humidity q_L . The nonlinear terms involving the small-scale humidity have maximum values over the ocean and are the dominant added value to the time-fluctuation part. The nonlinear terms involving the small-scale wind are weaker than the ones involving the small-scale humidity and tend to be strongest over the continent near the

topography. Finally the large-scale part of the time fluctuation of the vertically integrated moisture flux divergence TF is that which is best reproduced by the CRCM, having the maximum spatial correlation between CRCM and NCEP with values above 0.90.

According to the discussion about the effect of vertical and temporal resolution, it is important to use enough pressure levels in the low levels when computing the moisture budget, especially if one wants to look at the added value of the CRCM as the vertical resolution is mainly affecting the small scales. As for the temporal resolution, one must keep in mind that by using 6-h output data, the variance in scales smaller than 2000 km is underestimated, but overall it is much more important to use a sufficient vertical resolution to obtain reasonable values for the divergence of the moisture flux when calculated over pressure levels. The use of 6-hourly output data introduces some approximations, but these are necessary to reduce data volume for long time series. The temporal resolution issue might be exacerbated in summer in order to properly capture the diurnal cycle of moisture over the continents.

These conclusions have been drawn from only one

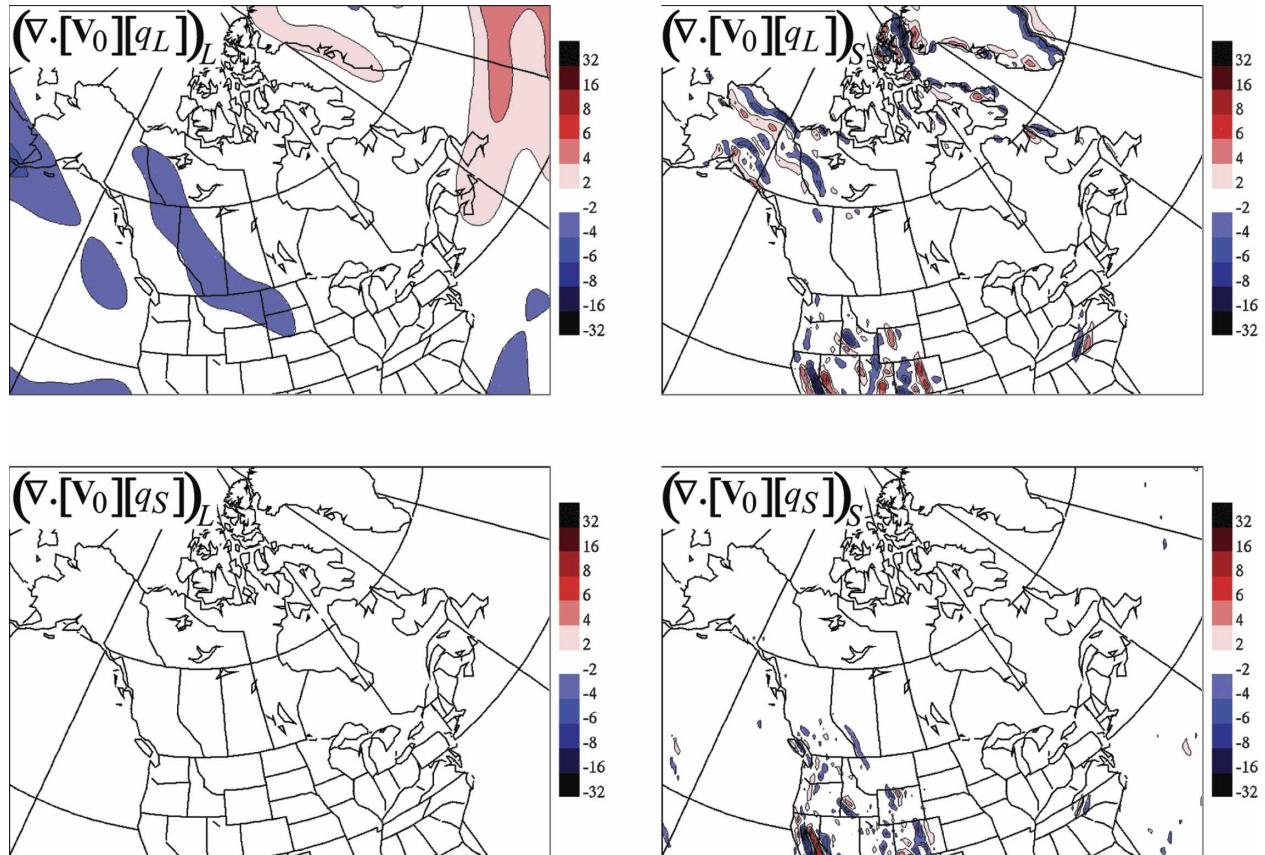


FIG. 18. Scale decomposition of the two terms $\nabla \cdot [\mathbf{V}_0][q_L]$ and $\nabla \cdot [\mathbf{V}_0][q_S]$ into (left) large and (right) small scales.

winter month of simulation. A 25-yr seasonal analysis is ongoing for both winter and summer seasons. We do not expect the results for the winter season to be very different from the monthly analysis. However, the summer season will probably be very different as convection is very strong during this period. Topographic forcing may no longer be the major small-scale forcing over the continent. It would also be very interesting to apply our methodology over the Mississippi basin to study the central United States flood of June–July 1993.

Acknowledgments. This research was supported in part by the Canadian Foundation for Climate and Atmospheric Sciences (CFCAS) and the Ouranos Consortium. The authors are grateful to the staff of the CRCM Network and of the Ouranos Simulation group for their assistance and to Mr. Claude Desrochers for maintaining an efficient local computing facility.

REFERENCES

- Boer, G. J., 1982: Diagnostic equations in isobaric coordinates. *Mon. Wea. Rev.*, **110**, 1801–1820.
- , 1994: Mean and transient spectral energy and enstrophy budgets. *J. Atmos. Sci.*, **51**, 1765–1779.
- , and T. G. Shepherd, 1983: Large-scale two-dimensional turbulence in the atmosphere. *J. Atmos. Sci.*, **40**, 164–184.
- Caya, D., and R. Laprise, 1999: A semi-implicit semi-Lagrangian regional climate model: The Canadian RCM. *Mon. Wea. Rev.*, **127**, 341–362.
- Chen, Q.-S., and Y.-H. Kuo, 1992: A harmonic-sine series expansion and its application to partitioning and reconstruction problems in a limited area. *Mon. Wea. Rev.*, **120**, 91–112.
- Davies, H. C., 1976: A lateral boundary formulation for multi-level prediction models. *Quart. J. Roy. Meteor. Soc.*, **102**, 405–418.
- Denis, B., J. Côté, and R. Laprise, 2002a: Spectral decomposition of two-dimensional atmospheric fields on limited-area domains using the discrete cosine transform (DCT). *Mon. Wea. Rev.*, **130**, 1812–1829.
- , R. Laprise, D. Caya, and J. Cote, 2002b: Downscaling ability of one-way nested regional climate models: The Big-Brother experiment. *Climate Dyn.*, **18**, 627–646.
- Errico, R. M., 1985: Spectra computed from a limited area grid. *Mon. Wea. Rev.*, **113**, 1554–1562.
- , 1987: A comparison between two limited-area spectral analysis schemes. *Mon. Wea. Rev.*, **115**, 2856–2861.
- Gal-Chen, T., and R. C. Somerville, 1975: On the use of a coordinate transformation for the solution of the Navier–Stokes equation. *J. Comput. Phys.*, **17**, 209–228.
- Kalnay, E., and Coauthors, 1996: The NCEP/NCAR 40-Year Reanalysis Project. *Bull. Amer. Meteor. Soc.*, **77**, 437–471.

- Lambert, S. J., 1984: A global available potential energy-kinetic energy budget in terms of the two-dimensional wavenumber for the FGGE year. *Atmos.–Ocean*, **22**, 265–282.
- , 1987: Spectral energetics of the Canadian Climate Centre general circulation model. *Mon. Wea. Rev.*, **115**, 1295–1304.
- Laprise, R., 2003: Resolved scales and nonlinear interactions in limited-area models. *J. Atmos. Sci.*, **60**, 768–779.
- , D. Caya, A. Frigon, and D. Paquin, 2003: Current and perturbed climate as simulated by the second-generation Canadian Regional Climate Model (CRCM-II) over northwestern North America. *Climate Dyn.*, **21**, 405–421.
- Peixoto, J., and A. Oort, 1992: *Physics of Climate*. American Institute of Physics, 520 pp.
- Tatsumi, Y., 1986: A spectral limited-area model with time dependent lateral boundary conditions and its application to a multi-level primitive equation model. *J. Meteor. Soc. Japan*, **64**, 907–923.
- Trenberth, K. E., and A. Solomon, 1993: Implications of global atmospheric spatial spectra for processing and displaying data. *J. Climate*, **6**, 531–545.
- van Tuyl, A. H., and R. M. Errico, 1989: Scale interaction and predictability in a mesoscale mode. *Mon. Wea. Rev.*, **117**, 495–517.